INTERNATIONAL JOURNAL FOR NUMERICAL METHODS IN FLUIDS
Int. J. Numer. Meth. Fluids 2003; **42**:813–837 (DOI: 10.1002/fld.540)

A non-linear k–ε model with realizability for prediction of flows around bluff bodies

Ichiro Kimura[1,*,†] and Takashi Hosoda[2]

[1]*Faculty of Environmental and Information Sciences, Yokkaichi University, 1200 Kayo-cho, Yokkaichi-shi, Mie-ken, 512-8512, Japan*
[2]*Department of Civil Engineering, Kyoto University, Yoshida, Sakyo-ku, Kyoto 606-8501, Japan*

SUMMARY

The incompressible flow around bluff bodies (a square cylinder and a cube) is investigated numerically using turbulence models. A non-linear k–ε model, which can take into account the anisotropy of turbulence with less CPU time and computer memory than RSM or LES, is adopted as a turbulence model. In tuning of the model, the model coefficients of the non-linear terms are adjusted through the examination of previous experimental studies in simple shear flows. For the tuning of the coefficient in the eddy viscosity ($=C_\mu$), the realizability constraints are derived in three types of basic 2D flow patterns, namely, a simple shear flow, flow around a saddle and a focal point. C_μ is then determined as a function of the strain and rotation parameters to satisfy the realizability. The turbulence model is first applied to a 2D flow around a square cylinder and the model performance for unsteady flows is examined focussing on the period and the amplitude of the flow oscillation induced by Karman vortex shedding. The applicability of the model to 3D flows is examined through the computation of the flow around a surface-mounted cubic obstacle. The numerical results show that the present model performs satisfactorily to reproduce complex turbulent flows around bluff bodies. Copyright © 2003 John Wiley & Sons, Ltd.

KEY WORDS: turbulence model; non-linear k–ε model; realizability; flow around a bluff body; Karman vortex

1. INTRODUCTION

An incompressible turbulent flow around a bluff body is an important topic for various engineering and scientific fields and has been studied extensively with numerical approaches as well as experimental ones. Recent rapid advances of computer technology has made it possible to use some new computational approaches such as LES or DNS. For instance, Murakami [1] and Murakami and Izuka [2] pointed out the superiority of LES to RANS type models for the prediction of the flows around a building. However, RANS type turbulence models, such

---

[*] Correspondence to: Ichiro Kimura, Faculty of Environmental and Information Sciences, Yokkaichi University, 1200 Kayo-cho, Yokkaichi-shi, Mie-ken 512-8512, Japan.
[†] E-mail: kimura@yokkaichi-u.ac.jp

Received August 2001
Revised 22 January 2003

as two equation models or Reynolds stress models, are still valid especially for engineering purposes because they require less CPU time and computer memory than LES or DNS [3]. Therefore, the clarification of the possibility and the limitation of RANS models should be still paid attention to. From the viewpoint of computational efficiency and model simplicity, non-linear $k-\varepsilon$ models are attractive for the computations of flows influenced by anisotropy of turbulence. We have verified the applicability of modified non-linear $k-\varepsilon$ models containing effects of the strain parameter S and rotation parameter Ω to a flow with a side-discharge [4], a flow around a square cylinder [5] and a compound open channel flow [6].

It is essential for turbulence models to satisfy the realizability conditions [7]. In this study, the realizability conditions are examined in three types of 2D basic flow patterns (the simple shear flow, the flow around a saddle point and the flow around a focal point), and restrictions for the coefficient in eddy viscosity $(=C_\mu)$ are derived on an S–Ω plane.

The present turbulence model is applied to the flow around bluff bodies and model performance is discussed. The standard $k-\varepsilon$ model is also applied for the purpose of comparison. The particular flows presented in this paper are the flows around a square cylinder and a surface-mounted cubic obstacle. Both flows contain separation, reattachment, recirculation and stagnation. The applicability to the 2D flow around a square cylinder is examined first focussing on the Karman vortex shedding. The laboratory test conducted by Lyn *et al.* [8, 9] is employed as the test case. The 3D behaviour of the present model is tested through the examination of the calculated results for the flow around a surface mounted cubic obstacle studied experimentally by Larousse *et al.* [10]. In both cases, the computed results are compared with the experimental data for both mean and turbulent quantities.

2. THE NON-LINEAR $k-\varepsilon$ MODEL

2.1. Basic equations

The basic equations in a $k-\varepsilon$ model for an incompressible flow are
(Continuity equation)

$$\frac{\partial U_i}{\partial x_i}=0 \tag{1}$$

(Momentum equation)

$$\frac{\partial U_i}{\partial t}+\frac{\partial U_j U_i}{\partial x_j}=g_i-\frac{1}{\rho}\frac{\partial p}{\partial x_i}+\frac{\partial -\overline{u_i u_j}}{\partial x_j}+v\frac{\partial^2 U_i}{\partial x_j^2} \tag{2}$$

($k-\varepsilon$ equations)

$$\frac{\partial k}{\partial t}+\frac{\partial k U_j}{\partial x_j}=-\overline{u_i u_j}\frac{\partial U_i}{\partial x_j}-\varepsilon+\frac{\partial}{\partial x_j}\left\{\left(\frac{v_t}{\sigma_k}+v\right)\frac{\partial k}{\partial x_j}\right\} \tag{3}$$

$$\frac{\partial \varepsilon}{\partial t}+\frac{\partial \varepsilon U_j}{\partial x_j}=-C_{\varepsilon 1}\frac{\varepsilon}{k}\overline{u_i u_j}\frac{\partial U_i}{\partial x_j}-C_{\varepsilon 2}\frac{\varepsilon^2}{k}+\frac{\partial}{\partial x_j}\left\{\left(\frac{v_t}{\sigma_\varepsilon}+v\right)\frac{\partial \varepsilon}{\partial x_j}\right\} \tag{4}$$

where x_i is the spatial co-ordinate, t the time, U_i the averaged velocities, u_i the turbulent velocities, p the averaged pressure, ρ the density of fluid, k the averaged turbulent energy,

ε the averaged turbulent energy dissipation rate, ν_t the eddy viscosity coefficient, ν the molecular kinematic viscosity coefficient and σ_k, σ_ε, $C_{\varepsilon 1}$, $C_{\varepsilon 2}$ are the model constants ($\sigma_k = 1.0$, $\sigma_\varepsilon = 1.3$, $C_{\varepsilon 1} = 1.44$, $C_{\varepsilon 2} = 1.92$ are used).

2.2. Constitutive equations

In the standard $k-\varepsilon$ model, Reynolds stress tensors are evaluated by the linear constitutive equation

$$-\overline{u_i u_j} = \nu_t S_{ij} - \frac{2}{3} k\delta_{ij}, \quad S_{ij} = \frac{\partial U_i}{\partial x_j} + \frac{\partial U_j}{\partial x_i}, \quad \nu_t = C_\mu \frac{k^2}{\varepsilon} \tag{5}$$

where C_μ is usually set to a constant ($= 0.09$). Since the standard $k-\varepsilon$ model does not take into account the anisotropy of the Reynolds stresses, the model cannot be applied to flows induced by the anisotropy, such as the secondary currents of the second kind. This shortcoming can be overcome to some extent by introducing a non-linear expression in the constitutive equation (5) as follows [11]:

$$-\overline{u_i u_j} = \nu_t S_{ij} - \frac{2}{3} k\delta_{ij} - \frac{k}{\varepsilon} \nu_t \sum_{\beta=1}^{3} C_\beta \left(S_{\beta ij} - \frac{1}{3} S_{\beta\alpha\alpha}\delta_{ij} \right) \tag{6}$$

$$\nu_t = C_\mu \frac{k^2}{\varepsilon} \tag{7}$$

$$S_{1ij} = \frac{\partial U_i}{\partial x_\gamma}\frac{\partial U_j}{\partial x_\gamma}, \quad S_{2ij} = \frac{1}{2}\left(\frac{\partial U_\gamma}{\partial x_i}\frac{\partial U_j}{\partial x_\gamma} + \frac{\partial U_\gamma}{\partial x_j}\frac{\partial U_i}{\partial x_\gamma} \right), \quad S_{3ij} = \frac{\partial U_\gamma}{\partial x_i}\frac{\partial U_\gamma}{\partial x_j} \tag{8}$$

Non-linear terms in (6) are equivalent to the following formula with strain and rotation tensors by Pope [12] and Gatski and Speziale [13].

$$\alpha_1(S_{il}\Omega_{lj} + \Omega_{il}S_{lj}) + \alpha_2(S_{il}S_{lj} - \tfrac{1}{3} S_{km}S_{mk}\delta_{ij}) + \alpha_3(\Omega_{il}\Omega_{lj} - \tfrac{1}{3}\Omega_{km}\Omega_{mk}\delta_{ij}) \tag{9}$$

where

$$S_{ij} = \frac{\partial U_i}{\partial x_j} + \frac{\partial U_j}{\partial x_i}, \quad \Omega_{ij} = \frac{\partial U_i}{\partial x_j} - \frac{\partial U_j}{\partial x_i}$$

The relations of the coefficients in Equations (8) and (9) are

$$C_1 = -2\alpha_1 + \alpha_2 - \alpha_3, \quad C_2 = 2(\alpha_2 + \alpha_3), \quad C_3 = 2\alpha_1 + \alpha_2 - \alpha_3 \tag{10}$$

The coefficient C_μ is now a function of the strain parameter S and the rotation parameter Ω used in the previous studies of Pope [12] and Gatski and Speziale [13]:

$$S = \frac{k}{\varepsilon}\sqrt{\frac{1}{2}\left(\frac{\partial U_i}{\partial x_j} + \frac{\partial U_j}{\partial x_i} \right)^2}, \quad \Omega = \frac{k}{\varepsilon}\sqrt{\frac{1}{2}\left(\frac{\partial U_i}{\partial x_j} - \frac{\partial U_j}{\partial x_i} \right)^2} \tag{11}$$

2.3. Tuning of coefficients C_1–C_3

In coefficients of the non-linear terms in (6), the C_1–C_3, should be carefully determined because they are expected to influence the physical accuracy and numerical performance of the model. In this study, the coefficients are adjusted through the consideration of the anisotropy in simple shear flows reported in previous experimental studies by Champagne *et al.* [14] (CHC) and Harris *et al.* [15] (HGC).

In a simple shear flow described by

$$U_1 = U_1(x_2), \quad U_2 = U_3 = 0, \quad \frac{dU_1}{dx_2} > 0 \tag{12}$$

the strain parameter becomes equivalent to the rotation parameter as follows:

$$S = \Omega = M = \frac{k}{\varepsilon}\frac{dU_1}{dx_2}, \quad M = \max(S, \Omega) \tag{13}$$

Diagonal components of the dimensionless Reynolds stress tensors are

$$\frac{\overline{u_1u_1}}{k} = \frac{2}{3} + C_\mu \frac{2C_1 - C_3}{3} M^2 \tag{14a}$$

$$\frac{\overline{u_2u_2}}{k} = \frac{2}{3} + C_\mu \frac{2C_3 - C_1}{3} M^2 \tag{14b}$$

$$\frac{\overline{u_3u_3}}{k} = \frac{2}{3} - C_\mu \frac{C_3 + C_1}{3} M^2 \tag{14c}$$

The anisotropic tensors m_{ij} are defined by

$$m_{ij} = \frac{\overline{u_iu_j}}{k} - \frac{2}{3}\delta_{ij} \tag{15}$$

The ratio of the turbulence energy production term P_k to the dissipation rate ε is

$$\alpha = \frac{P_k}{\varepsilon} = -\frac{\overline{u_1u_2}}{\varepsilon}\frac{dU_1}{dx_2} = C_\mu M^2 \tag{16}$$

We have proposed the following values for C_1–C_3 from our previous studies in compound open channel flows [4] and flows around a square cylinder [5]:

$$C_1 = 0.4, \quad C_2 = 0, \quad C_3 = -0.13 \tag{17}$$

Diagonal components of the anisotropic tensor m_{11}, m_{22}, m_{33} derived from (14), (15) and (17) are plotted against α in Figure 1 (dotted lines). The agreement with the experimental results becomes worse with increasing α. We therefore introduce the following functional expressions for C_1–C_3.

$$C_1 = 0.4 f_M(M), \quad C_2 = 0, \quad C_3 = -0.13 f_M(M) \tag{18}$$

where $f_M(M)$ is the function

$$f_M(M) = \frac{1}{1 + 0.01M^2} \tag{19}$$

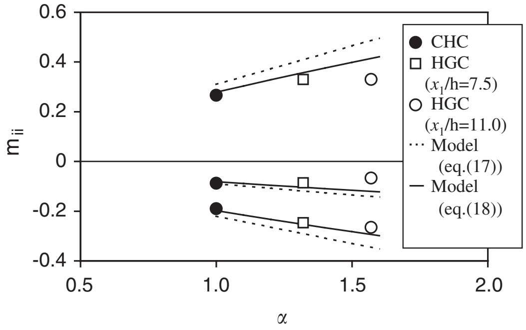

Figure 1. Comparison between Equations (17) and (18) for $C_1 - C_3$.

The relation between m_{ii} and α in (18) with (19) is also plotted against α in Figure 1 (solid lines). The results from (18) and (19) agree with the experimental results better than those from (17).

3. CONSIDERATIONS OF THE REALIZABILITY

3.1. *Realizability inequalities*

It is essential for turbulence models to satisfy some realizability conditions [7]. The realizability inequalities for 3D turbulent flow fields are:

$$\overline{u_i u_i} \geqslant 0 \tag{20a}$$

$$\overline{u_i u_i} \cdot \overline{u_j u_j} \geqslant \overline{u_i u_j}^2 \quad (i \neq j) \tag{20b}$$

$$\det \begin{bmatrix} \overline{u_1 u_1} & \overline{u_1 u_2} & \overline{u_1 u_3} \\ \overline{u_2 u_1} & \overline{u_2 u_3} & \overline{u_2 u_3} \\ \overline{u_3 u_1} & \overline{u_3 u_2} & \overline{u_3 u_3} \end{bmatrix} \geqslant 0 \tag{20c}$$

Einstein's summation rule is not applied in (20). In a 2D averaged flow field, (20c) coincides with (20b). In this study, the functional form for $C_\mu(S,\Omega)$ is determined through the examination of the realizability conditions in 2D averaged flows. In the following, the restrictions on C_μ from conditions (20a) and (20b) are derived for three types of basic 2D flow patterns, i.e. simple shear flow, the flow around a saddle point and the flow around a focal point.

3.2. *Analysis of inequality (20a)*

3.2.1. Simple shear flow. Diagonal components of the Reynolds stress tensors should be non-negative as

$$\frac{\overline{u_1 u_1}}{k} = \frac{2}{3} + \frac{C_\mu(2C_1 - C_3)}{3} M^2 \geqslant 0 \tag{21a}$$

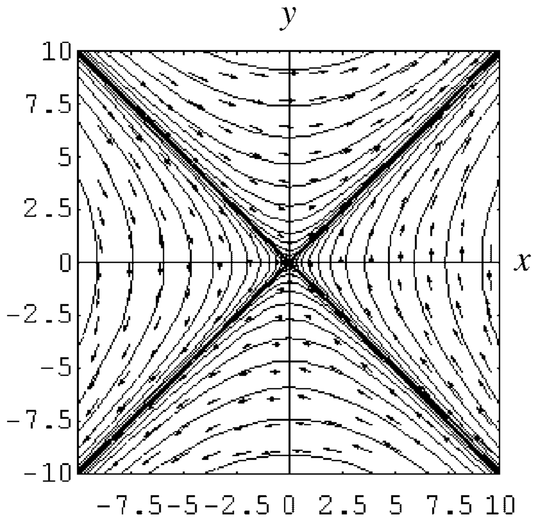

Figure 2. Solution curves at a saddle point ($a=d=0$, $b=c=1$).

$$\frac{\overline{u_2u_2}}{k}=\frac{2}{3}+\frac{C_\mu(2C_3-C_1)}{3}M^2\geqslant 0 \tag{21b}$$

Equation (21a) is satisfied regardless of M when C_1 and C_3 are given by (18). Equation (21b) requires

$$C_\mu\leqslant\frac{2}{(C_1-2C_3)M^2}=\frac{2}{0.66f_M(M)M^2} \tag{22}$$

3.2.2. Flow around a saddle point. The 2D flow field around a singular point can be described by

$$U_1=\frac{\mathrm{d}x_1}{\mathrm{d}t}=ax_1+bx_2 \tag{23a}$$

$$U_2=\frac{\mathrm{d}x_2}{\mathrm{d}t}=cx_1+\mathrm{d}x_2 \tag{23b}$$

The condition satisfied at a saddle point is

$$ad-bc<0 \tag{24}$$

Figure 2 shows an example of solution curves and a vector field around a saddle point. The continuity equation applied to (23a) and (23b) can be rewritten as

$$\mathrm{div}\,\mathbf{V}=a+d=0,\quad \mathbf{V}=\begin{pmatrix}U_1\\U_2\end{pmatrix} \tag{25}$$

and then the eigenvalues λ and eigenvectors μ are given by

$$\lambda = \pm\sqrt{a^2 + bc} \tag{26a}$$

$$\mu_1 = \left[1/N_1, \left.\frac{-1+\sqrt{a^2+bc}}{c}\right/ N_1\right], \quad \mu_2 = \left[1/N_2, \left.\frac{-1-\sqrt{a^2+bc}}{c}\right/ N_2\right] \tag{26b}$$

where

$$N_1 = \frac{\sqrt{2a^2 + c^2 + bc - 2a\sqrt{a^2+bc}}}{|c|}, \quad N_2 = \frac{\sqrt{2a^2 + c^2 + bc + 2a\sqrt{a^2+bc}}}{|c|} \tag{27}$$

When $a = 0$, two eigenvectors in (26b) become symmetrical for x_1-axis and the angle between two vectors can be arbitrarily changed by moving the values of b and c. If (20a) and (20b) are satisfied at $a = 0$, $\overline{u_i u_i}$ becomes non-negative under the rotation of the co-ordinate system. Therefore, the following analysis is carried out only in case of $a = 0$.

S and Ω can be described using a, b, c, d as

$$S = \frac{k}{\varepsilon}\sqrt{(b+c)^2}, \quad \Omega = \frac{k}{\varepsilon}\sqrt{(b-c)^2} \tag{28}$$

Expressions (24) and (28) and $a = 0$ yield the relation

$$bc = \frac{\varepsilon^2}{4k^2}(S^2 - \Omega^2) > 0 \tag{29}$$

which indicates an inequality between S ($\geqslant 0$) and Ω ($\geqslant 0$) where

$$S > \Omega \tag{30}$$

Then, $\overline{u_2 u_2}$ can be described using S and Ω as

$$\overline{u_2 u_2} = \frac{2}{3}k + \frac{1}{3}C_\mu k C_1\left[\left\{\frac{3}{4}(S \pm \Omega)^2 - \frac{1}{2}(S^2 + \Omega^2)\right\}\right.$$
$$\left. + \frac{1}{4}C_2(S^2 - \Omega^2) + C_3\left\{(S^2 + \Omega^2) - \frac{3}{4}(S \pm \Omega)^2\right\}\right] \tag{31}$$

(i) *When the double signs in* (31) *are positive*: Equation (31) can be rewritten in the form

$$\frac{\overline{u_2 u_2}}{k} = \frac{2}{3} + \frac{1}{3}C_\mu[E_1 S^2 + E_2 \Omega^2 + E_3 S\Omega] \geqslant 0 \tag{32}$$

where

$$E_1 = \frac{C_1 + C_2 + C_3}{4}, \quad E_2 = \frac{C_1 - C_2 + C_3}{4}, \quad E_3 = \frac{3(C_1 - C_3)}{2} \tag{33}$$

When (18) and (19) are substituted into (32) and (33), (21b) is always satisfied regardless of S and Ω.

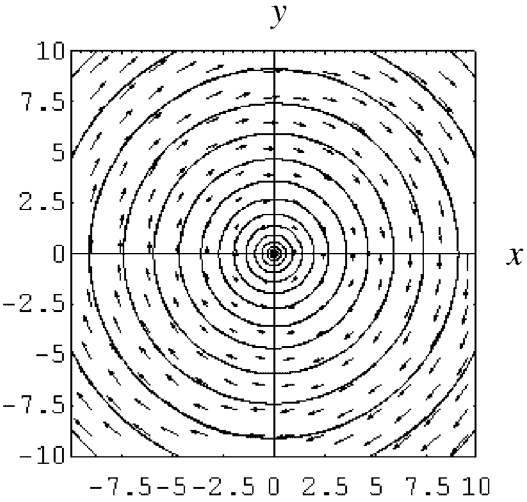

Figure 3. Solution curves at a focal point ($a=d=0$, $b=1$, $c=-1$).

(ii) *When the double signs in* (31) *are negative*: Equation (31) can be rewritten in the form

$$\frac{\overline{u_2u_2}}{k}=\frac{2}{3}+\frac{1}{3}C_\mu f(S,\Omega)\geqslant 0, \quad f(S,\Omega)=E_1S^2+E_2\Omega^2-E_3S\Omega \tag{34}$$

When $f(S,\Omega)\geqslant 0$, the constraint in (21b) is always satisfied. When $f(S,\Omega)<0$, (21b) requires

$$C_\mu \leqslant -\frac{2}{f(S,\Omega)} \tag{35}$$

and $-f(S,\Omega)$ becomes maximum in the limit of $\Omega\to S$, so that

$$-f(S,\Omega)=(C_1-2C_3)M^2 \tag{36}$$

Inequality (35) with (36) coincides with the constraint in (22) in the simple shear flow.

The constraint in $\overline{u_1u_1}$ can be proved to be equivalent to that in $\overline{u_2u_2}$.

3.2.3. Flow around a focal point.

At a focal point, the eigenvalues λ in (26a) become pure imaginary numbers. Hence, the relations between a, b, c and d at a focal point are

$$a+d=0 \tag{37a}$$

$$ad-bc>0 \tag{37b}$$

Figure 3 shows an example of solution curves and a vector field at a focal point. Equation (37a) coincides with the continuity equation ($\operatorname{div}\mathbf{V}=0$). The following analysis is carried out for case $a=0$ in the same way as the analysis at a saddle point. The inequality between S and Ω becomes

$$S<\Omega \tag{38}$$

The constraint in a focal point coincides with (35) under restriction (38). In the limit of $S \to \Omega$, the constraint agrees with Equation (22) in a simple shear flow.

The constraint in $\overline{u_1u_1}$ is equivalent to that in $\overline{u_2u_2}$.

3.3. Analysis of inequality (20b)

3.3.1. Simple shear flow. The Reynolds stress component $\overline{u_1u_2}$ is

$$\frac{\overline{u_1u_2}}{k} = -C_\mu M, \quad M = \max(S, \Omega) \tag{39}$$

Equation (20b) for the case $(i=1, j=2)$ becomes

$$C_\mu^2[9S^2 + (2C_1^2 + 2C_3^2 - 5C_1C_3)S^4] - C_\mu 2(C_1 + C_3)S^2 - 4 \leqslant 0 \tag{40}$$

which places the following restriction on C_μ:

$$C_\mu \leqslant \frac{(C_1 + C_3)S + \sqrt{(C_1 + C_3)^2S^2 + 4[9 + (2C_1^2 + 2C_3^2 - 5C_1C_3)S^2]}}{9S + (2C_1^2 + 2C_3^2 - 5C_1C_3)S^3} \tag{41}$$

3.3.2. Flow around a saddle point. Reynolds stress components $\overline{u_1u_1}$, $\overline{u_2u_2}$ and $\overline{u_1u_2}$ can be described using S and Ω as

$$\frac{\overline{u_1u_1}}{k} = \frac{2}{3} + \frac{1}{3} C_\mu[C_1A_1 + C_2A_2 + C_3A_3] \tag{42a}$$

$$\frac{\overline{u_2u_2}}{k} = \frac{2}{3} + \frac{1}{3} C_\mu[C_1A_3 + C_2A_2 + C_3A_1] \tag{42b}$$

$$\frac{\overline{u_1u_2}}{k} = \mp C_\mu S \tag{42c}$$

where

$$A_1 = \tfrac{1}{4}(S^2 + \Omega^2) \mp \tfrac{2}{3} S\Omega, \quad A_2 = \tfrac{1}{4}(S^2 - \Omega^2), \quad A_3 = \tfrac{1}{4}(S^2 + \Omega^2) \pm \tfrac{2}{3} S\Omega, \quad S > \Omega \tag{43}$$

From (42) and (43), the realizability inequality (20b) becomes

$$\begin{aligned} &[9S^2 - (C_1A_1 + C_2A_2 + C_3A_3)(C_1A_3 + C_2A_2 + C_3A_1)]C_\mu^2 \\ &\quad - 2[(A_1 + A_3)(C_1 + C_3) + 2A_2C_2]C_\mu - 4 \leqslant 0 \end{aligned} \tag{44}$$

The left-hand side of (44) becomes zero when

$$C_{\mu 1} = \frac{(A_1 + A_3)(C_1 + C_3) + 2A_2C_2 - \sqrt{[(A_1 + A_3)(C_1 + C_3) + 2A_2C_2]^2 + 4B_1}}{B_1} \tag{45a}$$

$$C_{\mu 2} = \frac{(A_1 + A_3)(C_1 + C_3) + 2A_2C_2 + \sqrt{[(A_1 + A_3)(C_1 + C_3) + 2A_2C_2]^2 + 4B_1}}{B_1} \tag{45b}$$

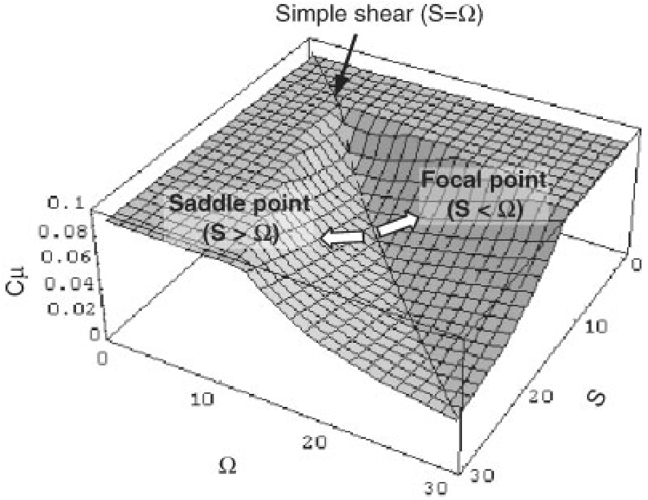

Figure 4. Realizability conditions in Equation (20a) for C_μ on an S–Ω plane.

where

$$B_1 = 9S^2 - (C_1A_1 + C_2A_2 + C_3A_3)(C_1A_3 + C_2A_2 + C_3A_1) \neq 0 \tag{46}$$

When C_1, C_2 and C_3 are given by (18) and (19), B_1 is always positive. Therefore, (44) yields the following restriction for C_μ:

$$C_\mu \leqslant C_{\mu 2} \tag{47}$$

3.3.3. Flow around a focal point. At a focal point ($S < \Omega$), the restriction from realizability (20b) takes the same form as the result at a saddle point in (47) with (45b) and (46).

3.4. Constraints for C_μ on a S–Ω plane

Realizability conditions for (20a) and (20b) in the simple shear flow, the flow around a saddle point and the flow around a focal point are plotted on a S–Ω plane in Figures 4 and 5, respectively. To satisfy the realizability, C_μ should be lower than the curved surface in these figures. These figures indicate that the model with constant C_μ ($= 0.09$) does not satisfy the realizability constraint. When $C_\mu(S, \Omega) = C_\mu(M)$ is assumed, the constraint in the simple shear flow ($M = S = \Omega$) becomes very restrictive. The constraints in the simple shear flow in each equation are shown in Figure 6 in solid lines.

In this study, the following two forms for C_μ are tested:

$$C_\mu(M) = \min\left[0.09, \frac{0.3}{1 + 0.4M}\right] \tag{48}$$

$$C_\mu(M) = \min\left[0.09, \frac{0.3}{1 + 0.09M^2}\right] \tag{49}$$

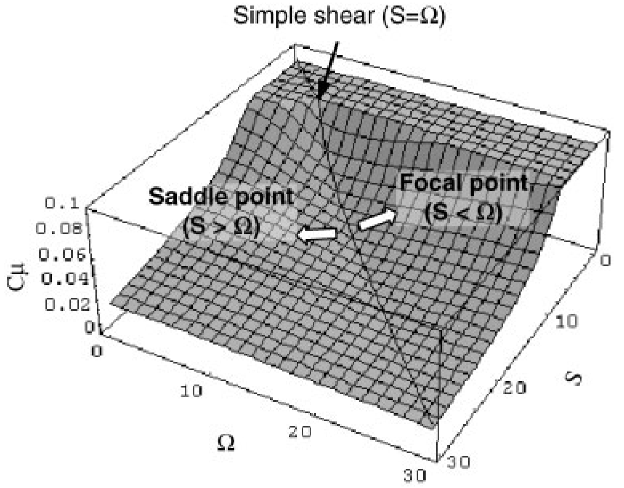

Figure 5. Realizability conditions in Equation (20b) for C_μ on an $S-\Omega$ plane.

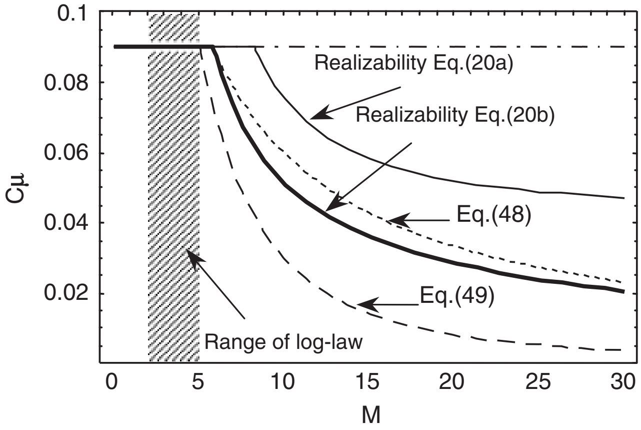

Figure 6. Relation between C_μ and M in a simple shear flow.

where $C_\mu(M)$ in both Equations (48) and (49) satisfies inequality (20a) and takes a constant value ($=0.09$) in flows which satisfy the log-law, as discussed later. Note that $C_\mu(M)$ in (48) does not satisfy inequality (20b).

3.5. $C_\mu(M)$ in the log-law region

We examine the characteristics of the function $C_\mu(M)$ in (48) and (49) in the log-law region. The velocity distribution of the flow in a log-law region on a smooth bed is described as

$$\frac{U(y)}{U_*} = \frac{1}{\kappa} \ln y^+ + A_S, \quad y^+ = \frac{yU_*}{\nu} \tag{50}$$

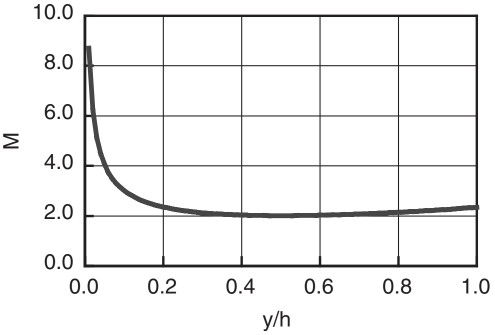

Figure 7. Relation between M and y/h in the velocity distribution in the log-law region.

where $U_* =$ the friction velocity, $\kappa = 0.41$ and $A_s = 5.3$. Nezu and Nakagawa [16] suggested the following semi-theoretical formulae for k and ε in open channel flows:

$$\frac{k}{U_*^2} = 4.78 \exp\left(-2\frac{y}{h}\right) \tag{51a}$$

$$\frac{\varepsilon h}{U_*^2} = 9.76 \frac{\exp(-3y/h)}{\sqrt{y/h}} \tag{51b}$$

where h is the depth. From Equations (50) and (51), a relation between M $(=S=\Omega)$ and y/h is derived as

$$M = 0.346 \frac{1}{\kappa}\sqrt{\frac{h}{y}} \exp\left(\frac{y}{h}\right) \tag{52}$$

Figure 7 shows a plot of the relation in (52). When the order of the Reynolds number is 10^3-10^5, the range of M becomes 2–5. From (48) and (49), it is seen that in this log-law region, $C_\mu(M)$ takes the constant value of 0.09.

4. APPLICATION OF THE TURBULENCE MODEL TO THE 2D FLOW AROUND A SQUARE CYLINDER

4.1. Outline of the calculated flow field

To verify the performance of the present turbulence model, it is applied to a 2D flow around a square cylinder with Karman vortex shedding. Numerical simulations are performed under the conditions of the laboratory test by Lyn *et al.* [8, 9], which was conducted in closed water channel (for $Re = 2.2 \times 10^4$). The flow domain in the calculation is shown in Figure 8.

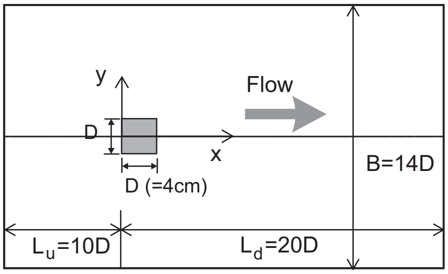

Figure 8. Computational flow domain for the square cylinder problem.

4.2. Turbulence models

The following four turbulence models are tested:

Run 1 (Standard $k-\varepsilon$ model): The Reynolds stress tensors are evaluated as in Equation (5) with a constant value of C_μ $(=0.09)$.

Run 2: The Reynolds stress tensors are evaluated by non-linear equations (6)–(8), in which all model coefficients are set to be constants (see (17)):

$$C_1 = 0.4, \quad C_2 = 0, \quad C_3 = -0.13, \quad C_\mu = 0.09 \tag{53}$$

Run 3: The coefficients C_1, C_2, C_3 and C_μ in Equation (6) are evaluated as functions of strain parameter S and rotation parameter Ω in (18), (19) and (48) as follows:

$$C_1 = \frac{0.4}{1+0.01M^2}, \quad C_2 = 0, \quad C_3 = \frac{-0.13}{1+0.01M^2}, \quad C_\mu = \min\left(0.09, \frac{0.3}{1+0.4M}\right) \tag{54}$$

Run 4: The coefficients in Equation (6) are evaluated in (18), (19) and (49) as follows:

$$C_1 = \frac{0.4}{1+0.01M^2}, \quad C_2 = 0, \quad C_3 = \frac{-0.13}{1+0.01M^2}, \quad C_\mu = \min\left(0.09, \frac{0.3}{1+0.09M^2}\right) \tag{55}$$

The difference between Runs 3 and 4 is only in the functional form for $C_\mu(M)$.

4.3. Discretization of the basic equations

The basic equations were discretized using the finite volume method on a staggered grid with the MAC method [17]. The QUICK scheme was applied to the convection terms and central differencing was used for the diffusion terms in the momentum equations. A Hybrid central upwind scheme [18] was applied to the k and ε equations. The equations were discretized in fully explicit form. The second-order Adams–Bashforth scheme was used for time integration of each equation. The pressure field was solved using an iterative procedure at each time step via the SOLA algorithm [19].

4.4. Boundary and initial conditions

The numerical grid used in the calculation is a stretched rectangular one shown in Figure 9. Franke *et al.* [20] pointed out that the distance of the first grid point away from the wall has

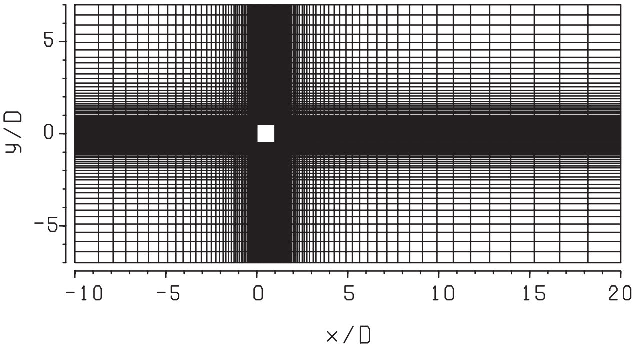

Figure 9. Numerical Grid.

a particularly strong influence on the results. Taking into account the use of the wall function approach, the first grid point should be placed out of the viscous sub-layer. In this study, the smallest distance of the grid lines near the cylinder is chosen to be 2 mm ($=D/20$) based on some previous calculations. Under this condition, the maximum value of the dimensionless distance $y^+(=U_*\Delta/v$, U_*: the friction velocity, Δ: the distance between the side-wall and the first definition point of the velocity) at the side-wall of the cylinder becomes around 40. The maximum stretching of successive cells is limited to $0.9 \leqslant q_x$, $q_y \leqslant 1.1$, where $q_x = \Delta x_i/\Delta x_{i-1}$ and $q_y = \Delta y_j/\Delta y_{j-1}$ to suppress the influence of grid stretching. The number of the grid-points is 112 in x direction and 92 in y direction.

The wall function approach was taken for the wall boundary conditions. At the down-stream end of the computational domain, a zero streamwise gradient was specified for velocities, k and ε. At the inlet boundary, the level of k was chosen to match the turbulence levels (=2%) in the experiment by Lyn *et al.* The value of ε at the inlet was determined from the value of k at the inlet by Equation (5) after specifying the ratio $v_t/v = 10$ [21].

At the beginning of the calculations, $U = U_0 = 55\,\mathrm{cm/s}$, $V = 0$, $k = k_{\mathrm{in}}$ and $\varepsilon = \varepsilon_{\mathrm{in}}$ (k_{in} and $\varepsilon_{\mathrm{in}}$ are the values of k and ε at the inlet boundary) were specified over the whole computational domain as initial condition.

4.5. Numerical results

In all sets of the calculated results, Karman vortex shedding was generated. The Strouhal number ($St = fD/U_0$, f: frequency) of the vortex shedding in all Runs was within the range $0.144 - 0.146$ and was about 11% larger than the experimental measured result ($St = 0.13$).

Figure 10 shows the distribution of the non-dimensional velocity component U/U_0 along the x-axis. The length of the recirculation zone calculated in Run 1 is too long and the recovery of the velocity at the downstream region of the recirculation zone is too slow. The recirculation zone in Run 2 is a little larger than the experimental one. On the other hand, Run 3 underpredicts the length of the recirculation zone. Run 4 accurately calculated not only the length of the recirculation zone but also the whole distribution of the velocity. For further evaluation of the present model, the result by Run 4 is compared with the result by the RNG non-linear k–ε model by Yakhot *et al.* [22] in Figure 11. In the RNG model, the following

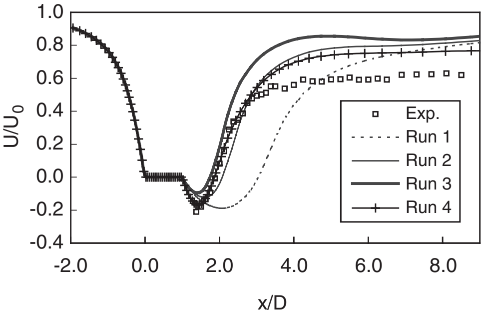

Figure 10. U/U_0 on x-axis for Runs 1–4.

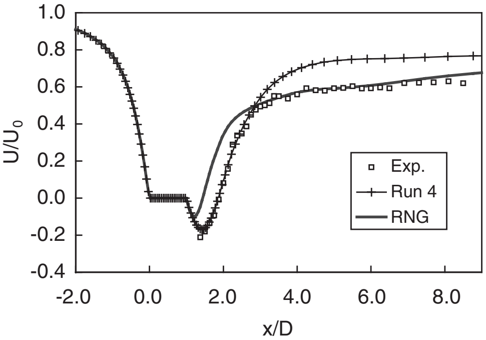

Figure 11. U/U_0 on x-axis for Run 4 and RNG model [22].

term is added to the right-hand side of ε Equation (4):

$$-\frac{C_\mu S^3(1-S/S_0)}{1+\beta S^3}\frac{\varepsilon^2}{k} \tag{56}$$

where $C_\mu = 0.085$, $\beta = 0.012$ and $S_0 = 4.38$. The constants in k and ε equations have been determined without any ad hoc approaches through RNG (renormalization group) theory as $C_{\varepsilon 1} = 1.42$, $C_{\varepsilon 2} = 1.68$, $\sigma_k = \sigma_\varepsilon = 0.719$. The RNG model underpredicts the length of the recirculation behind the cylinder. However, it reproduces the profile of U/U_0 at $x/D > 2.5$ well.

The comparison of the non-dimensional turbulence energy k' $(=k/U_0^2)$ is shown in Figure 12. The calculated values of k' in all models are considerably smaller than the experimental one. Similar discrepancies of k are indicated in the 2D calculations with a linear $k-\varepsilon$ model by Bosch and Rodi [21] and with RSM by Franke and Rodi [23]. Bosch and Rodi [21] pointed out that the low-frequency modulation due to 3D large-scale structure in the laboratory test cannot be captured by the 2D calculations, and the calculated k' thereby becomes much smaller than the experimental one.

The distribution of k' near the impinging region in Figure 12 is enlarged in Figure 13. Runs 1 and 2 have large values of k' just before the impinging region. The production of k in Runs 3 and 4 is suppressed. This figure demonstrates that the non-linear $k-\varepsilon$ model with the effects of S and Ω can suppress the excessive production of k near the impinging region and the second-order non-linear terms in (6) have no effect on suppression.

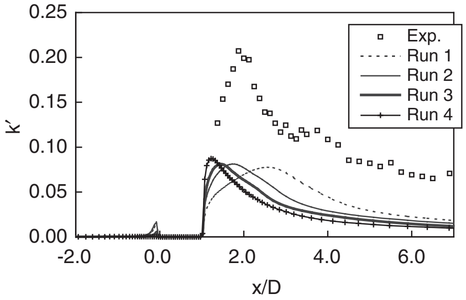

Figure 12. $k' = k/U_0^2$ along x-axis.

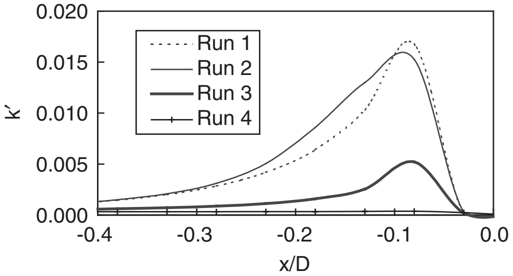

Figure 13. $k' = k/U_0^2$ along the x-axis near the impinging region.

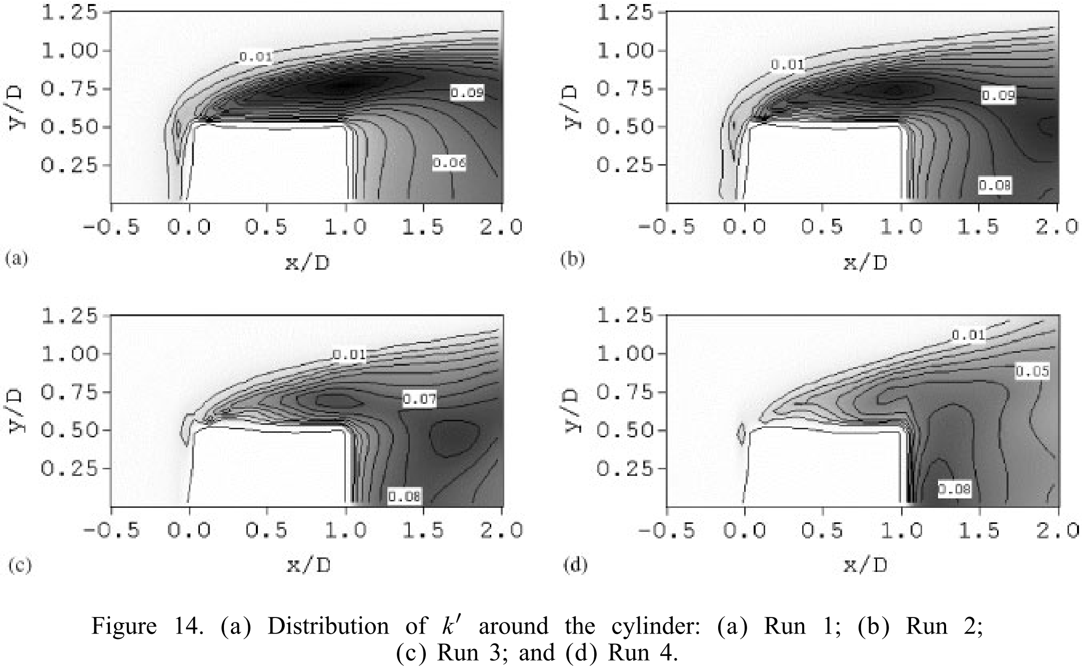

Figure 14. (a) Distribution of k' around the cylinder: (a) Run 1; (b) Run 2; (c) Run 3; and (d) Run 4.

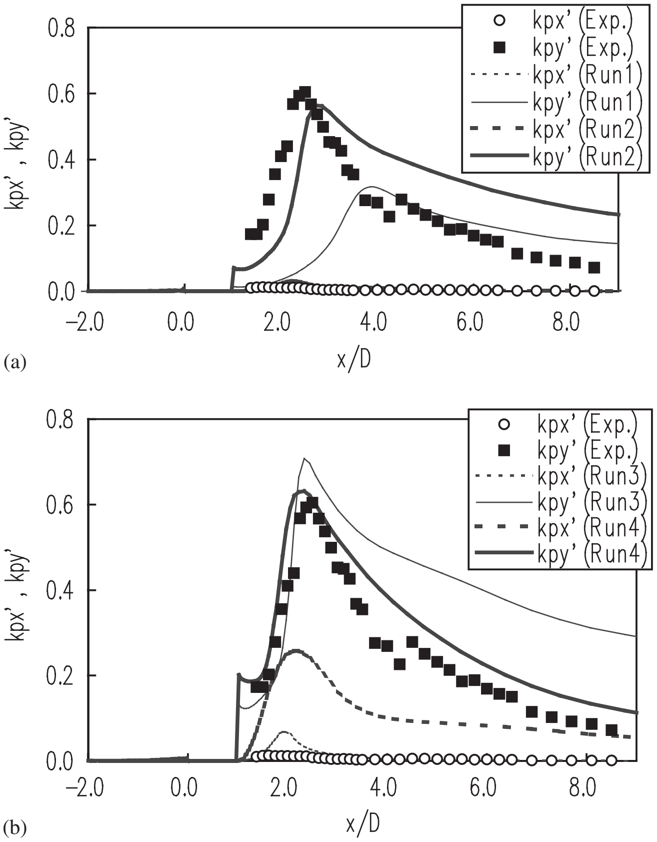

Figure 15. k'_{px} and k'_{py} along the x-axis: (a) Runs 1 and 2; (b) Runs 3 and 4.

Figures 14(a)–14(d) show the distributions of time-averaged turbulence energy k' near the cylinder. The distributions from Runs 1 and 2 are similar and have two peaks at the side and near the leading edge of the cylinder. In the results of Runs 3 and 4, values of k' around the cylinder are smaller than those of Runs 1 and 2.

Figure 15(a) and 15(b) show the periodic part of the non-dimensional fluctuation energies in x-component, k_{px}, and in y component, k_{py}, along the x-axis. Every model overpredicts the peak value of k_{px}. Run 4 particularly gives very large values of k_{px} compared with the experiment. In the temporal variation of the streamwise velocity of Run 4, considerable deviation from periodicity was detected (Figure 16). It is assumed that the excessive production of k_{px} of Run 4 is caused by the irregularity of the velocity fluctuations. As for k_{py}, the peak value of Run 1 is very small and that of Run 2 is also a little smaller than the experimental value. Runs 3 and 4 predicted the peak value of k_{py} well and the longitudinal distribution of Run 4 was in good agreement with experiment over the whole region of the plot.

Figure 17 shows the comparison of the non-dimensional total fluctuation energy k'_t (periodic part + turbulence part) along the x-axis. The outcome of Run 1 is significantly smaller than the experimental one. Although the peak value of Run 4 is slightly larger than that of the

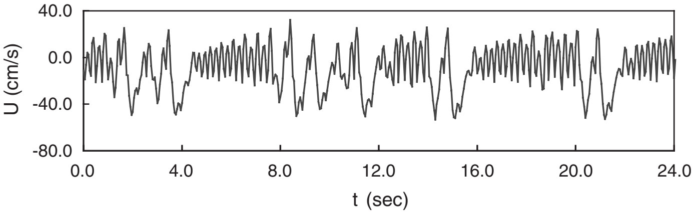

Figure 16. Temporal variation of U (Run 4, at $x/D = 6$).

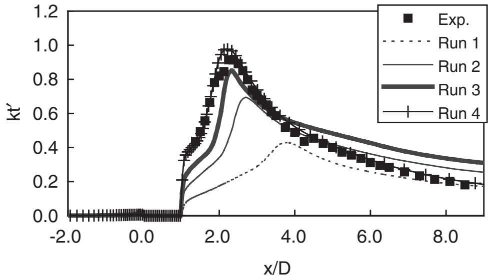

Figure 17. Total fluctuation energy along the x-axis for Runs 1–4.

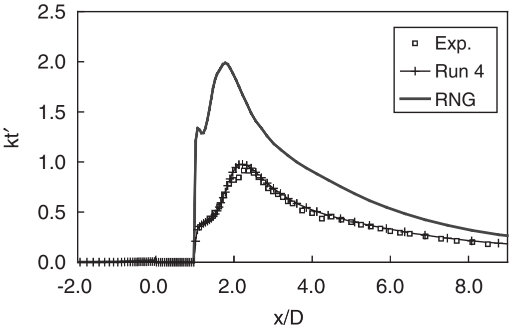

Figure 18. Total fluctuation energy along the x-axis for Run 4 and RNG model [22].

experiment, the computations of Run 4 reproduces the distribution of total fluctuation energy very well. Figure 18 shows the comparison of the results of Run 4 and the RNG model [22]. This figure shows that the RNG model significantly overpedicts the total fluctuation energy behind the cylinder.

The drag coefficient C_D and the lift coefficient C_L are important parameters in the flows around bluff bodies. In this case, the time-mean lift coefficient in each Run becomes zero because the time-mean flow is symmetrical for the x-axis. The drag coefficients in averaged flow fields of different turbulence models are listed in Table I. This table shows that the turbulence models that underpredict the length of the recirculation behind the cylinder, yield

Table I. Drag coefficients of different turbulence models.

	Run 1	Run 2	Run 3	Run 4	Experiment
Drag coefficient C_D	1.66	1.93	2.05	2.09	2.1

Table II. Calculation times for different turbulence models (beginning with the initial conditions).

	Run 1	Run 2	Run 3	Run 4
CPU time (s)	4982	3131	3609	3645
Rate against Run 1	1.00	0.63	0.72	0.73

Table III. Calculation times for different turbulence models (beginning from $t = 120$ s).

	Run 1	Run 2	Run 3	Run 4
CPU time (s)	1848	2202	2231	2391
Rate against Run 1	1.00	1.19	1.21	1.29

a smaller value of C_D. The value of C_D of Run 4 is in good agreement with the experimental data.

The numerical results in the 2D field indicate that the non-linear model of Run 4, which is the only realizable of the 4 models employed here, simulates most accurately both the mean and unsteady flow features with vortex shedding. The model of Run 4 reproduces the total fluctuation energy well, though the model underpredicts the turbulence energy. It should be noted that the division of the energy between the turbulence and directly simulated components in Run 4 disagrees with the division between the random and periodic components in the laboratory test.

The computational times for different turbulence models are also investigated as shown in Tables II and III. The computational times for the period of one vortex shedding ($= 0.5$ s) are measured on an IBM compatible personal computer (CPU: Pentium IV, 1.8 GHz, RAM: 256MB). Table II shows the computational times beginning from $t = 0$s (the initial conditions) and Table III shows those beginning from $t = 120$ s (fully periodic phase). Table II shows that the computational time for Run 1 is the largest in spite of its simplicity. The reason is as follows. It has been pointed out that one of the shortcomings of the standard $k-\varepsilon$ model is its large numerical viscosity. At the beginning of the calculation from the initial conditions, a separation bubble is formed behind the cylinder. During this process, the pressure field behind the cylinder changes rapidly. The calculation of Run 1 requires much time for the iteration of the pressure field during this process because of its large numerical viscosity. Since the calculation times in Table III are in fully periodic phase and are not affected by the initial conditions, those values reflect the complexity of the models. The difference in the calculation times between Runs 1 and 2 is due to the presence of the second-order terms in Run 2. Runs 3 and 4 take more calculation time than Run 2 because they require the calculation of the strain and rotation parameters.

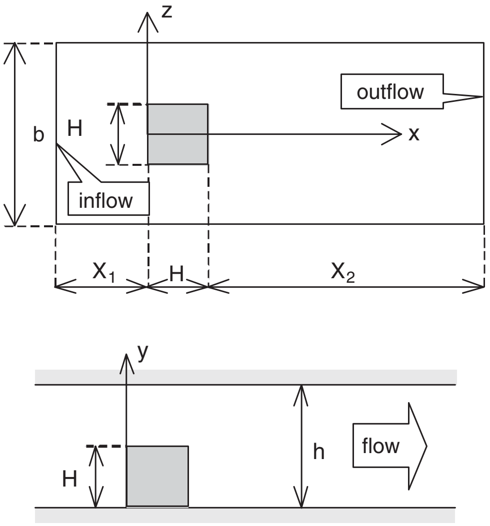

Figure 19. Plane and vertical view of the flow domain for the 3D cubic obstacle.

5. 3D CALCULATIONS OF THE FLOW AROUND A SURFACE-MOUNTED CUBIC OBSTACLE

5.1. Experimental data

The flow around a surface-mounted cubic obstacle has full 3D characteristics with separation and reattachment. The flow is therefore suitable for the testing of turbulence models. In this study, the LDA measurements of the flow around a surface-mounted cube performed by Larousse *et al.* [10] were employed to assess. The plane and vertical sections of the flow domain in the laboratory test are shown in Figure 19 ($h = 5$ cm and $H = 2.5$ cm). The Reynolds number based on the channel height ($Re = U_0 h/\nu$, $U_0 =$ the bulk velocity) is 10^5.

5.2. Outline of the numerical procedure

The numerical procedure in the 3D computation is the same as the one used in the 2D computation described in Section 4.3, except the spatial dimension of the basic equations.

The numerical grid used in the calculation is a stretched rectangular one. The smallest distance of the grid lines near the cube is 1.25 mm ($= H/20$). The number of the grid-points is 69 in the x direction, 26 in the y direction and 52 in the z direction. The length of the flow domain upstream of the cube is $X_1 = 5H$, and downstream of the cube is $X_2 = 14H$ (The definition of X_1 and X_2 is shown in Figure 19).

Three turbulence models, i.e. those of Runs 1, 2 and 4 described in Section 4.2 are employed in the calculations.

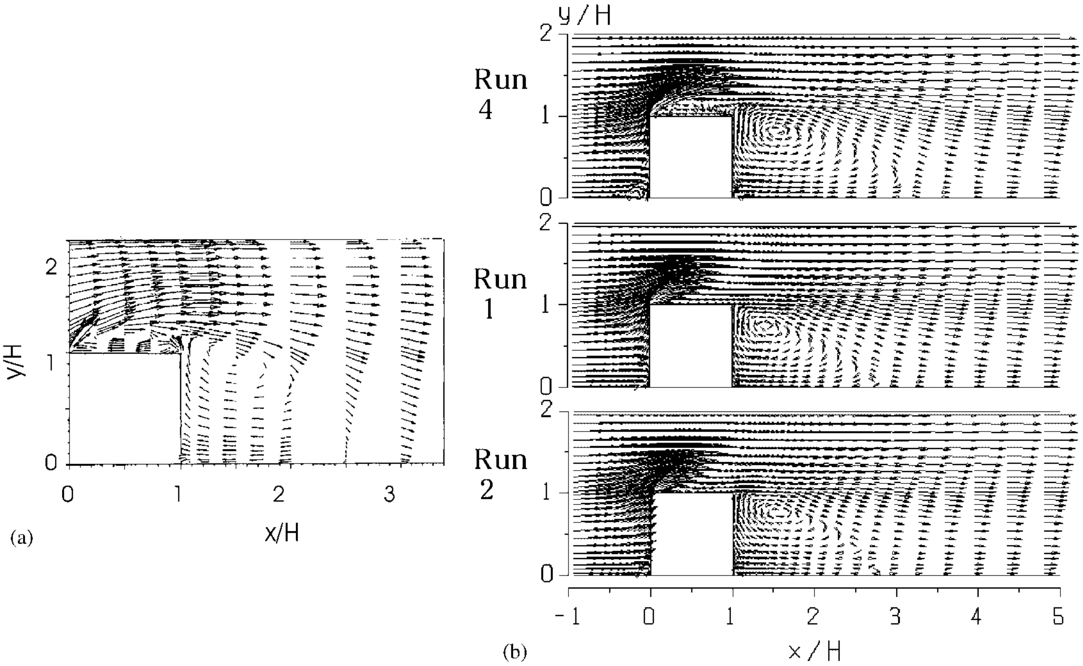

Figure 20. Flow patterns in the vertical section along the x-axis: (a) experiment and (b) calculation.

5.3. *Numerical results and discussion*

Figure 20 shows the comparison of flow patterns for a vertical section along the x-axis. In the experimental measurements, a recirculation zone is generated in the downstream region of the cube and the reattachment point of the separated flow is near $x/H=3$. Another recirculation is generated at the top-surface of the cube. In the numerical results, the recirculation at the top-surface of the cube was reproduced only by Run 4 and the other two models could not reproduce it. The reattachment length at the downstream of the cube by Run 4 is slightly longer than that in the laboratory test.

Figure 21 shows the distributions of turbulence energy k around the cube in the numerical results. The turbulence energy at the front of the cube by Run 4 is much smaller than those of Runs 1 and 2. The effect of the suppression of k near the impinging region by Run 4, which was also pointed out in 2D calculation around a cylinder, is observed again in this figure. The maximum points of the turbulence energy by Runs 1 and 2 are located near the front corner of the cube, but those for Run 4 can be seen near the rear corner. Figure 22 shows the distributions of dimensionless turbulence energy k' $(=k/U_0^2)$ in y–z plane in the downstream region of the cube $(x/H=1.25)$. This figure also demonstrates the influence of turbulence modelling in the distribution of turbulence energy. The values of Runs 1 and 2 are smaller than the experimental data because the maximum points are shifted to the upstream direction. The distribution of k' of Run 4 is in good agreement with the experiment.

Figure 23 shows the flow patterns for the two cross-sections at $x/H=1.75$ and $x/H=5.3$. In the experimental measurements at $x/H=1.75$, a vortex in a clockwise direction, which is a

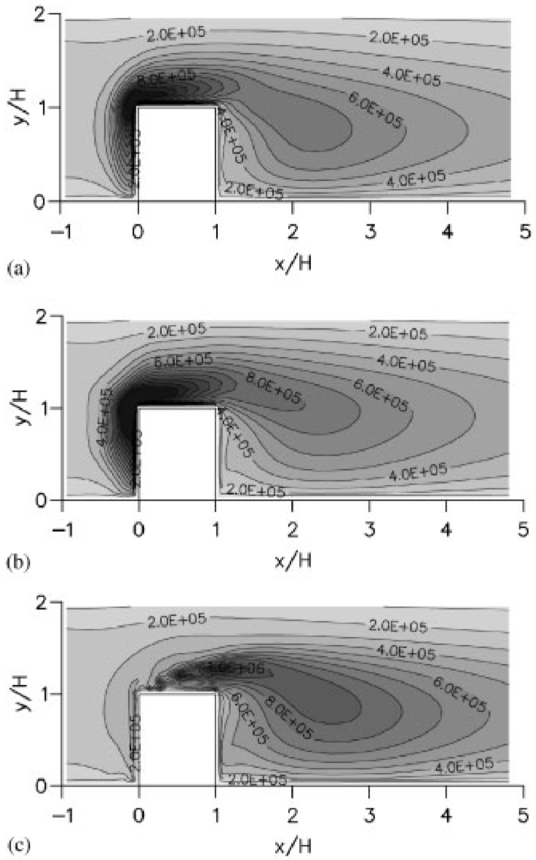

Figure 21. Turbulence energy distributions around the cube along the x-axis: (a) Run 1; (b) Run 2 and (c) Run 4.

part of the horseshoe vortex, formed around the cube, having been generated near the bottom. In the section at $x/H = 5.3$, the vortex becomes much larger than that at $x/H = 1.75$. Run 1 does not reproduce these cross-sectional vortex pattern. In the results of Run 2, the vortex is generated but is much smaller than that of the experiment. The calculated results of Run 4 are in good agreement with the experimental data.

The flow geometry with a cube presented here is simple but the flow generated around the cube is rather complex. The numerical results show that the realizable turbulence model of Run 4 is useful for predicting 3D complex turbulent flows with separation and reattachment around bluff bodies.

6. CONCLUDING REMARKS

A second-order, non-linear k–ε model, which includes some new considerations of realizability, is developed to predict flows around bluff bodies. The constraint of realizability, i.e. the

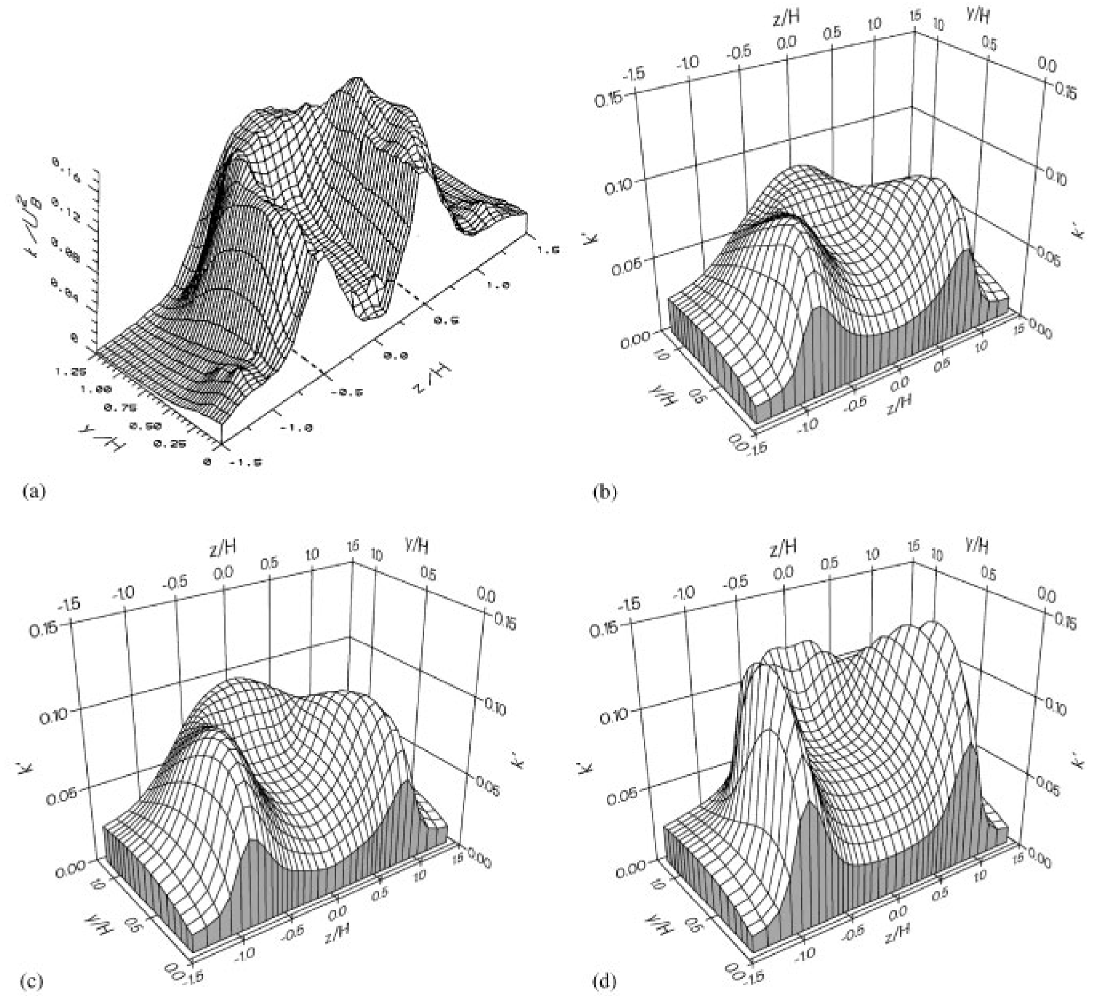

Figure 22. Turbulence energy distributions in the y–z plane at $x/H = 1.25$: (a) Experiment; (b) Run 1; (c) Run 2 and (d) Run 4.

non-negativity of the normal Reynolds stresses and the Schwarz' inequality between turbulent velocity correlations are derived for a simple shear, a saddle point and a focal point configuration. The coefficient C_μ is tuned as a function of the Strain parameter and the Rotation parameter to satisfy realizability. The coefficients of the non-linear terms, C_1, C_2 and C_3, were also calibrated carefully through the consideration of anisotropy of simple shear flows reported in experimental flow studies.

For the examination of the model performance, the turbulence model was applied to the 2D flow around a square cylinder and the 3D flow around a surface-mounted cubic obstacle. In the 2D calculation, the present model could reproduce the Karman vortex formation and the predicted total fluctuation energy due to the vortex shedding was in close agreement with the experiment, although the division of the energy between the turbulence and directly simulated

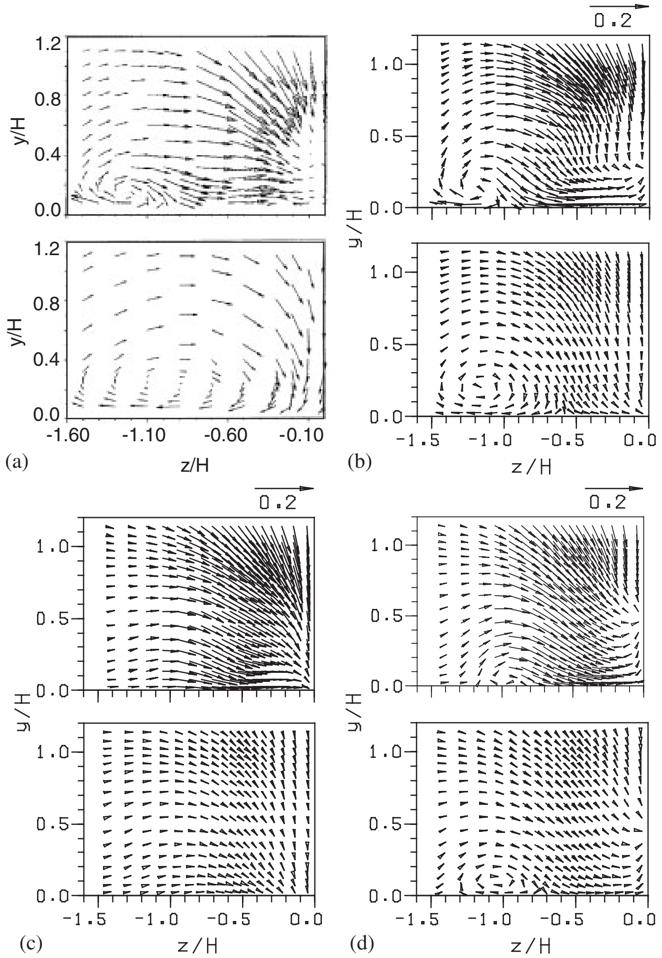

Figure 23. Cross-sectional flow patterns (upper: $x/H = 1.75$, lower: $x/H = 5.3$): (a) Experiment; (b) Run 4; (c) Run 1 and (d) Run 2.

components disagrees with the division between the random and periodic components in the laboratory test. In the 3D calculation around a cube, the complex flow features with separation and reattachment at each surface are qualitatively simulated. The calculated results, which are encouraging in both cases, show the applicability of the present model for the calculation of complex turbulent flows around bluff bodies in various engineering set-up.

REFERENCES

1. Murakami S. Computational wind engineering. *Journal of Wind Engineering and Industrial Aerodynamics* 1990; **36**:517–538.
2. Murakami S, Izuka S. CFD analysis of turbulent flow past squre cylinder using dynamic LES. *Journal of Fluids and Structures* 1990; **13**:1097–1112.
3. Tutar M, Holdø AE. Computational modelling of flow around a circular cylinder in sub-critical flow regime with various turbulence models. *International Journal for Numerical Methods in Fluids* 2001; **35**:763–784.

4. Hosoda T, Kimura I, Muramoto Y. Vortex formation processes in open channel flows with a side discharge by using the non-linear $k-\varepsilon$ model. *Proceedings of 11th Symposium on Turbulent Shear Flows*, Grenoble, vol. 2, 1997; 19.1–19.6.
5. Kimura I, Hosoda T. 3-D unsteady flow structures around rectangular column in open channels by means of non-linear $k-\varepsilon$ model. *Proceedings of 1st International Symposium on Turbulence and Shear Flow Phenomena*, Santa Barbara, USA, 1999; 1001–1006.
6. Hosoda T, Sakurai T, Kimura I, Muramoto Y. 3-D Computations of compound open channel flows with horizontal vortices and secondary currents by means of non-linear $k-\varepsilon$ model. *Journal of Hydroscience and Hydraulic Engineering* 1999; **17**(2):87–96.
7. Schumann U. Realizability of Reynolds-stress turbulence models. *Physics of Fluids* 1977; **20**:721–725.
8. Lyn DA. Vortex shedding past a square cylinder. *ERCOFTAC Fluid Dynamics Database* 1992; **43**.
9. Lyn DA, Einav W, Rodi W, Park J-H. A laser-doppler velocimetry study of ensemble-averaged characteristics of the turbulent near wake of a square cylinder. *Journal of Fluid Mechanics* 1995; **304**:285–319.
10. Larousse A, Martinuzzi R, Tropea C. Flow around surface-mounted, three-dimensional obstacles. *Turbulent Shear Flows*, vol. 8. Springer: New York, 1993; 127–139.
11. Yoshizawa A. Statistical analysis of the deviation of the Reynolds stress from its Eddy viscosity representation. *Physics of Fluids* 1984; **27**:1377–1387.
12. Pope SB. A more general effective viscosity hypothesis. *Journal of Fluid Mechanics* 1975; **72**:331–340.
13. Gatski TB, Speziale CG. On explicit algebraic stress models for complex turbulent flows. *Journal of Fluid Mechanics* 1993; **254**:59–78.
14. Champagne FH, Harris VG, Corrsin S. Experiments on nearly homogeneous turbulent shear flow. *Journal of Fluid Mechanics* 1970; **41**:81–139.
15. Harris VG, Graham JAH, Corrsin S. Further experiments in nearly homogeneous turbulent shear flow. *Journal of Fluid Mechanics* 1977; **81**:657–687.
16. Nezu I, Nakagawa H. Turbulence in open-channel flows. *IAHR Monograph*, Balkema, Rotterdam, 1993.
17. Amsden AA, Harlow FH. The SMAC method: a numerical technique for calculating incompressible fluid flows. *Los Alamos Scientific Report* LA-4370, 1970.
18. Spalding DB. A novel finite-difference formulation for differential expressions involving both first and second derivatives. *International Journal for Numerical Methods in Engineering* 1972; **4**:551–559.
19. Hirt CW, Nichols BD, Romero NC. SOLA—a numerical solution algorithm for transient fluid flows. *Los Alamos Scientific Report* LA-5852, 1975.
20. Franke R, Rodi W, Shönumg B. Numerical calculation of laminar vortex-shedding flow past cylinders. *Journal of Wind Engineering and Industrial Aerodynamics* 1993; **35**:237–257.
21. Bosch G, Rodi W. Simulation of vortex shedding past a square cylinder with different turbulence models. *International Journal for Numerical Methods in Fluids* 1998; **28**:601–616.
22. Yakhot V, Orszag SA, Thangham S, Gatski TB, Speziale CG. Development of turbulence models for shear flows by a double expansion technique. *Physics of Fluids* 1992; **4**(7):1510–1520.
23. Franke R, Rodi W. Calculation of vortex shedding past a square cylinder with various turbulence models. *Turbulent Shear Flows*, vol. 8. Springer: New York, 1993; 189–204.